International Journal of Nanomedicine

Dovepress
Taylor & Francis Group

Open Access Full Text Article

ORIGINAL RESEARCH

Copper-Based Metal-Organic Framework Nanoplatform for miRNA Delivery: Synergistic Antitumor Therapy

Maopu Tu[1,*], Xiaoyu Deng[2,*], Bin Lai[1,*], Jiao Liu[1], Yingzhou Tao[2], Shaohua Xu[2], Xiaodong Li[1], Xiaoqiang Niu[1], Zhixin Li[3], Jiahui Huang[2], Jiaxin Li[2], Shengxun Mao[1], Xi Ouyang[1], Jiaqing Cao[1]

[1]Department of Gastrointestinal Surgery, The Second Affiliated Hospital, Jiangxi Medical College, Nanchang University, Nanchang, Jiangxi, 330006, People's Republic of China; [2]Jiangxi University of Chinese Medicine, Nanchang, Jiangxi, 330004, People's Republic of China; [3]Institute for Advanced Study, Research Center for Differentiation and Development of TCM Basic Theory, Jiangxi University of Chinese Medicine, Nanchang, Jiangxi, 330004, People's Republic of China

*These authors contributed equally to this work

Correspondence: Jiaqing Cao; Xi Ouyang, Email ndefy89037@ncu.edu.cn; ouyangxi24@126.com

Background: Chemodynamic therapy (CDT) is a promising antitumor strategy that damages tumor cells by generating reactive oxygen species (ROS) to induce oxidative stress. However, antioxidant mechanisms in tumor cells greatly reduce CDT efficacy.

Methods: We propose using MOF-199 nanoparticles (NPs) with tumor microenvironment responsiveness as a carrier for miR-4521 to construct miR-4521@MOF-199 for cancer treatment. Polyacrylamide gel electrophoresis evaluated MOF-199's loading and protective capacity for miR-4521. In vitro and in vivo experiments assessed the system's antitumor effect and biosafety, with mechanisms explored.

Results: The miR-4521@MOF-199 NPs effectively protected and delivered miR-4521 to tumor cells. Within high-glutathione (GSH) tumor microenvironments, NP degradation released both miR-4521 and Cu^{2+}. The increased intracellular Cu^{2+} triggered tumor cell apoptosis via ROS-mediated CDT while activating cuproptosis through proteotoxic stress. Concurrently, miR-4521 disrupts the oxidative stress defense mechanisms of tumor cells by inhibiting FOXM1 expression, thereby enhancing the efficacy of CDT. Furthermore, the silencing of FOXM1 can further impede tumor progression through gene regulatory mechanisms. Experimental results demonstrate that miR-4521@MOF-199 exhibits potent antitumor efficacy and high biocompatibility via synergistic CDT, gene therapy, and cuproptosis.

Conclusion: This multifunctional nanosystem exhibits potent antitumor effects and low toxicity, providing a promising research direction for multimodal combinatorial cancer therapy based on CDT.

Keywords: chemodynamic therapy, microRNA, cuproptosis, gene therapy, nanoparticles, metal-organic frameworks

Introduction

Chemodynamic therapy (CDT) is an emerging tumor treatment strategy that harnesses metal ions (such as Fe^{2+}, Cu^{2+} and Mn^{2+}) to catalyze the conversion of overexpressed hydrogen peroxide (H_2O_2) within tumor cells into hydroxyl radicals (·OH), thereby inducing oxidative stress and achieving the killing of tumor cells.[1–3] However, compared to normal cells, tumor cells are characterized by a distinctive redox balance featuring elevated reactive oxygen species (ROS) levels coupled with upregulated antioxidant defense mechanisms.[4] This adaptive homeostasis significantly compromises the therapeutic efficacy of CDT.[5–7] Therefore, the development of nanocomposite systems that combine the functions of triggering CDT and inhibiting the antioxidant defense mechanism of tumor cells is expected to significantly enhance the therapeutic efficacy of CDT.

MicroRNAs (miRNAs) are endogenous ~22-nucleotide non-coding RNAs that inhibit translation or degrade target messenger RNAs (mRNAs) through sequence-specific binding, thereby critically regulating tumorigenesis and tumor

Received: 19 February 2025
Accepted: 18 June 2025
Published: 3 July 2025

Graphical Abstract

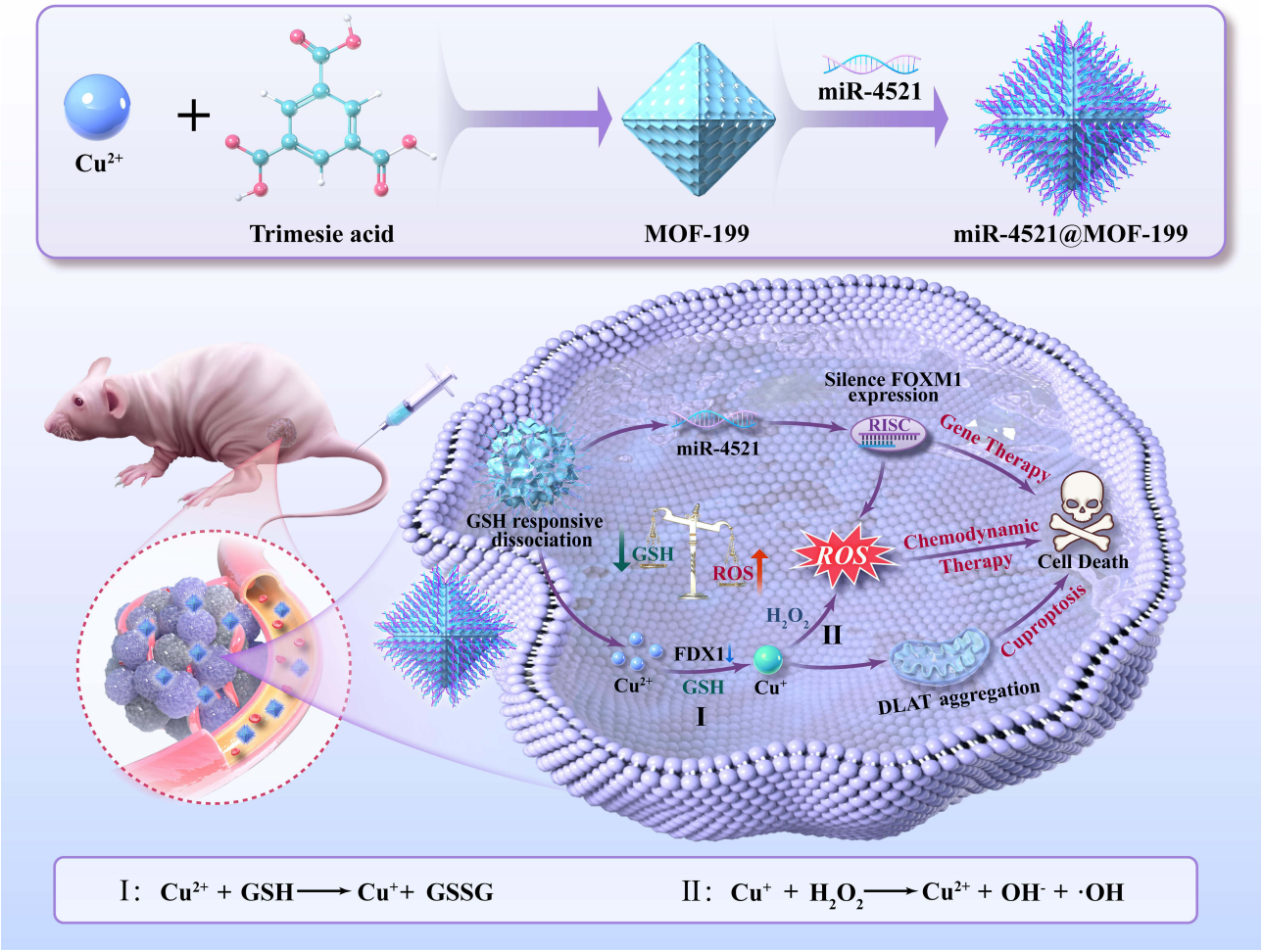

development.[8–11] Given their remarkable advantages, including minimal side effects and sustained efficacy, miRNAs have emerged as a cancer treatment strategy with promising prospects.[12,13] MiR-4521 is a miRNA derived from transfer RNA (tRNA). It specifically targets and inhibits the expression of FOXM1, thereby suppressing tumor progression and metastasis.[14–16] Furthermore, studies have demonstrated that FOXM1 plays a crucial role in the antioxidant defense mechanisms of tumor cells, exerting a potent antioxidant function by inhibiting the activity of various antioxidant enzymes.[17–19] Therefore, increasing the expression level of miR-4521 in tumor cells can not only exert the therapeutic effect of gene therapy but also significantly weaken the antioxidant defense mechanism of tumor cells and enhance the efficacy of CDT. However, problems such as nuclease degradation and poor cellular uptake have greatly hindered the clinical application of miRNAs.[20,21] To overcome this hindrance, researchers have developed viral vectors as well as nonviral vectors such as liposomes, micelles, and polyethyleneimine for the delivery of miRNA.[22,23] Regrettably, the immunogenicity triggered by viral vectors, along with their low loading capacity, poor RNA stability, and uncontrolled release characteristics of liposomes, micelles, and polyethyleneimine, severely limits their clinical translational potential.[24–26] Therefore, there is an increasing need for miRNA delivery systems characterized by superior biocompatibility, higher delivery efficiency, and controlled drug release.

Copper-based nanomaterials demonstrate significant potential in antibacterial and antitumor therapeutic applications owing to their high catalytic activity, distinctive electronic structures, and tailorable surface properties.[27,28] Particularly, copper-based metal-organic frameworks (MOFs)—coordination networks self-assembled from Cu^{2+} and organic ligands—exhibit exceptional biocompatibility combined with high drug-loading capacity and stimuli-responsive release profiles, making them versatile platforms for drug delivery.[29–31] Studies have shown that MOFs can encapsulate nucleic acids through electrostatic attraction and coordination interactions, thereby addressing critical challenges in nucleic acid delivery, such as enzymatic degradation and off-target effects.[32–34] In recent years, MOF-199 has attracted significant interest in cancer drug delivery due to its glutathione (GSH)-responsive degradation, which enables tumor microenvironment (TME)-triggered drug release specifically in GSH-rich conditions.[35–37] This characteristic is conducive to the targeted and controlled release of therapeutic drugs at the tumor site, thus elevating the precision of cancer treatment. In addition, after MOF-199 is dissociated by GSH, large amounts of Cu^{2+} are released.[38] Elevated intracellular concentration of Cu^{2+} can trigger a Fenton-like reaction to generate substantial amounts of toxic ROS for CDT.[39] At the same time, excess intracellular Cu^{2+} were reduced to more toxic Cu^{+} by ferredoxin 1 (FDX1), which inhibits the biosynthesis of iron-sulfur cluster proteins.[40] Moreover, Cu^{+} interferes with the mitochondrial tricarboxylic acid (TCA) cycle, disrupting normal metabolic pathways. This leads to the abnormal aggregation of dihydrolipoamide S-acetyltransferase (DLAT), subsequently triggering proteotoxic stress and inducing cell cuproptosis.[41,42]

Herein, a TME-responsive nucleic acid delivery nanosystem (termed miR-4521@MOF-199) was constructed by loading miR-4521 within the MOF-199 to enhance cancer therapy. miR-4521@MOF-199 nanoparticles (NPs) can accumulate in tumor tissues via the enhanced permeability and retention (EPR) effect,[43,44] while also protecting the miR-4521 from nuclease degradation in the bloodstream. Upon uptake by tumor cells, the overexpressed GSH facilitates the dissociation of miR-4521@MOF-199, leading to the release of miR-4521 and Cu^{2+}. On the one hand, Cu^{2+} is capable of triggering a Fenton-like reaction, thereby generating a substantial quantity of ROS and resulting in the apoptosis of tumor cells. On the other hand, Cu^{2+} binds to lipoylated mitochondrial enzymes, inducing abnormal oligomerization of DLAT. This triggers proteotoxic stress and ultimately leads to cuproptosis in tumor cells. Meanwhile, the increased miR-4521 in tumor cells significantly inhibits the expression of FOXM1, thereby weakening the antioxidant capacity of tumor cells and enhancing the therapeutic efficacy of CDT. In addition, the silencing of FOXM1 can also exert the effect of gene therapy to suppress tumor progression. Collectively, this work innovatively demonstrates that delivering miRNA to weaken tumor cells' oxidative defense enables synergistic CDT, gene therapy, and cuproptosis for effective and safe tumor suppression, providing a promising strategy for multimodal cancer combination therapy.

Materials and Methods

Materials

Trimesic acid (98%), copper nitrate trihydrate (99%), 5,5′-dithiobis-(2-nitrobenzoic acid) (DTNB, 98%), neocuproine (98%), methylene blue (MB, ≥70%), were procured from Aladdin (Shanghai, China). Total GSH colorimetric assay kit and calcein/PI assay kit were obtained from Elabscience (Wuhan, China). The ROS assay kit, mitochondrial membrane potential (MMP) assay kit with JC-1, Annexin V-FITC/PI apoptosis detection kit, Hoechst 33342, BCA protein assay kit and DLAT antibody were purchased from Solarbio (Beijing, China). Forkhead box M1 (FOXM1), ferredoxin-1 (FDX1) and beta-actin antibody were purchased from Proteintech (Wuhan China). miR-4521, FAM-labeled miR-4521 and Cy5-labeled miR-4521 were procured from GenePharma (Shanghai China).

Fabrication of MOF-199 NPs

The MOF-199 was fabricated with slight adjustments in accordance with the procedures reported in the literature.[36,45] Briefly, 289.9 mg of copper nitrate trihydrate and 252.2 mg of trimesic acid were separately added to 10 mL of a 1:1 (v/v) ethanol-deionized water mixture. Next, 250 μL of triethylamine was added slowly, and the mixture was stirred vigorously for 30 minutes at room temperature. The mixture was then washed twice with deionized water and three times with ethanol to remove any unreacted substances. Finally, the purified products were kept in ethanol at room temperature.

Fabrication of miR-4521@MOF-199 NPs

miR-4521@MOF-199 NPs were synthesized by combining 100 μL of MOF-199 (1 mg/mL) with 100 μL of miR-4521 at different concentrations (0, 200, 400, 800, 1600, and 3200 nM) at 4 °C. The weight ratios of miR-4521 to MOF-199 NPs were 0, 1/352, 1/176, 1/88, 1/44 or 1/22 (w/w)). After mixing, the remaining unloaded miR-4521 supernatant was removed by centrifugation to obtain the final miR-4521@MOF-199 NPs.

Characterizations

X-ray diffractometer (Bruker, D8 DISCOVER, Germany) was used to collect the powder XRD data. Scanning electron microscopy (SEM, ZEISS, Sigma 560, Germany), and transmission electron microscopy (TEM, JEM-F200, Japan) was used to investigate the morphology. The zeta potential and particle size distribution were determined via dynamic light scattering (DLS, Brookhaven, Omni, USA). Fourier-transform infrared spectroscopy (FT-IR) data were measured via an FTIR spectrometer (Thermo Fisher, Nicolet iS50, USA).

Protective Evaluation of miR-4521 in miR-4521@MOF-199 NPs

The stability of miR-4521 in miR-4521@MOF-199 was evaluated via polyacrylamide gel electrophoresis (PAGE). 4 ul of miR-4521 (10 μM) and miR-4521@MOF-199 NPs were incubated with 8 ul FBS for 0, 1, 2, or 4 h at 37 °C. Subsequently, the samples were collected and incubated with the nucleic acid dye. Next, the RNA stability of the different groups was analyzed by PAGE.

GSH Consumption Detection in vitro

MiR-4521@MOF-199 solutions (25, 50, 75, 100, and 200 μg/mL in PBS, pH 7.4) were individually mixed with 1 mM GSH solution and incubated for 30 min. After centrifugation at 6000 rpm for 3 min, 200 μL of the supernatant was added to 200 μL of DTNB solution (1 mM). Finally, the mixture absorbance at wavelengths ranging from 350 to 600 nm was monitored via UV-vis spectroscopy.

MiR-4521 Released from miR-4521@MOF-199 NPs

The release of FAM-labeled miR-4521 from miR-4521@MOF-199 NPs were analyzed under varying conditions (GSH, pH 7.4 and pH 6.0). FAM-miR-4521@MOF-199 was incubated with PBS containing GSH or pH-adjusted PBS (7.4/6.0), followed by centrifugation at designated time points to collect supernatants. Fluorescence intensity was quantified using a microplate reader (Tecan Infinite 200 PRO, Switzerland), and cumulative release amounts were calculated to compare effects of GSH and pH.

Detection of ROS Generation

The characteristic peak of MB at 665 nm decreases as the amount of ROS increases. Therefore, the ability to generate ROS was studied via the MB assay. First, GSH (1 mM) was mixed with miR-4521@MOF-199 (1 mg/mL) and then H_2O_2 (10 mM) was added. Subsequently, MB (5 μg/mL) was added to the mixed solution and incubated for 3 h. Finally, the absorbances of the different solutions were monitored via UV-vis spectrometry.

Cell Culture

Human gastric cancer cells (HGC-27 cells and AGS cells), human gastric mucosal epithelial cells (GES-1), and human umbilical vein endothelial cells (HUVEC cells) were provided by Procell Life Science & Technology Co., Ltd. (Wuhan, China). The cells were cultured in RPMI 1640 (Gibco) medium containing 10% fetal bovine serum (Gibco), 100 μg/mL streptomycin and 100 U/mL penicillin. The cells were incubated in an incubator (37 °C, 5% CO_2).

Cellular Uptake Assay

HGC-27 cell were seeded into confocal cell culture dishes and were treated with FAM-miR-4521@MOF-199 for different durations (0, 2, 4, and 8 h). After that, the cells were washed with PBS and fixed with 4% paraformaldehyde

and stained with Hoechst 33342 for 15 min. Finally, CLSM (Leica, Germany) was used to analyze the uptake of FAM-miR-4521@MOF-199 by HGC-27 cells. The experimental steps for observing the uptake of FAM-miR-4521@MOF-199 NPs by HGC-27 cells via flow cytometry were slightly different. HGC-27 cells were incubated with FAM-miR-4521 or FAM-miR-4521@MOF-199 for 8 h, washed with PBS, and analyzed by flow cytometry (Challenbio Fongcyte C2060, china) to quantify fluorescence intensity. In addition, after HGC-27 cells were treated with miR-4521@MOF-199 for 8 hours, they were washed with PBS, collected by centrifugation, and counted. Following digestion with nitric acid, the intracellular copper content was quantitatively detected by ICP-MS (Agilent 8900, japan).

In vitro Cytotoxicity Assessment

The HGC-27 cells, AGS cells, GES-1 cells and HUVEC cells were cultured in 96-well plates and incubated overnight. The cells were then treated with a series of various concentrations of miR-4521, MOF-199 and miR-4521@MOF-199 for 48 h. Subsequently, 10% CCK-8 solution was added to each well and incubated at 37°C for 2 h. Finally, after gently shaking for 10 min, the absorbance of the solution at 450 nm was measured.

Cell Apoptosis Assay

HGC-27 cells (2×10^5) were plated in 6-well plates and were treated differently for 48 h: (1) Control; (2) miR-4521; (3) MOF-199; (4) miR-4521@MOF-199. Subsequently, 5 μL of Annexin V - FITC and 5 μL of PI were added and incubated for 5 minutes in the dark. Finally, flow cytometry was used to detect cell apoptosis.

Assessment of Intracellular ROS

HGC-27 cells were plated in 6-well plates and treated differently for 8 h: (1) Control; (2) miR-4521; (3) MOF-199; (4) miR-4521@MOF-199. Subsequently, DCFH-DA (1 mL, 10 μM) was added to each well and placed in the incubator for a total of 20 min. Finally, inverted fluorescence microscopy and flow cytometry were used to analyze ROS production.

Mitochondrial Membrane Potential (MMP) Assay

HGC-27 (5×10^5) cells were plated in 6-well plates and treated differently for 8 h: (1) Control; (2) miR-4521; (3) MOF-199; (4) miR-4521@MOF-199. JC-1 fluorescent dye was added to each of the different groups respectively and incubated at 37 °C for 20 min. Finally, the flow cytometry was used to analyze the changes in the MMP of the cells in the different groups.

RT-qPCR

HGC-27 and GES-1 cells (5×10^5) were seeded into 6-well plates and incubated overnight. The cells were then treated differently for 48 h: (1) Control; (2) miR-4521; (3) MOF-199; (4) miR-4521@MOF-199. After washing the cells with PBS, the total RNA extraction kit was used to extract the total RNA from the cells. Reverse transcription was performed following the instructions of the Evo M-Mlv RT mix kit (Accurate, Changsha, China). Subsequently, quantitative PCR analysis was performed using the Premix Pro Taq HS qPCR Kit (SYBR Green). Amplification was monitored on QuantStudio™ 5 (Thermo Fisher; USA). The internal reference gene used was β-Actin, and the list of primers used is shown in Table S1.

Western Blotting

HGC-27 cells were plated in 6-well plates at a density of 5×10^5 and incubated overnight. The cells were then treated differently for 48 h: (1) Control; (2) miR-4521; (3) MOF-199; (4) miR-4521@MOF-199. Upon extraction of the total protein from the cells, the protein concentrations in various groups were determined via a BCA protein assay kit. After being diluted to an identical concentration, the proteins were subsequently fractionated via SDS-PAGE and then transferred onto a PVDF membrane. After being blocked, the PVDF membrane was incubated with primary antibodies against β-actin (1:15,000, Proteintech), FOXM1 (1:3000, Proteintech), and FDX1 (1:2000, Proteintech) overnight at 4 °C. Finally, the membranes were incubated with secondary antibody and visualized on an automatic chemiluminescence imaging system (BIO-RAD).

Establishment of the Animal Model

All animal experiments received approval from the Institutional Animal Ethics Committee (IAEC) of Nanchang University (NCULAE-20240801001), Nanchang, China. All experiments were performed in accordance with the National Institutes of Health Guide for the Care and Use of Laboratory Animals. Female BALB/c nude mice aged 4 weeks were procured from GemPharmatech Co., Ltd. After 1 week of rearing to adapt to the environment, 5×10^6 HGC-27 cells were subcutaneously injected into each mouse to establish the HGC-27 tumor model.

Biosafety Evaluation

Twelve female BALB/c nude mice were allocated into four groups. The mice in each group were respectively injected with saline, miR-4521, MOF-199, or miR-4521@MOF-199, and their body weights were monitored every 3 days. Upon the experiment's conclusion, blood samples were drawn from each mouse for routine blood examination and biochemical analyses. The principal organs of the mice were then harvested for H&E staining.

Live Animal Imaging and Biodistribution

HGC-27 tumor-bearing mice were intravenously injected with Cy5-miR-4521@MOF-199 (15 mg/kg). In vivo fluorescent images were obtained via IVIS®Lumina Series III (PerkinElmer, USA) at 1, 6, 12 and 24 h postinjection to evaluate the biodistribution of Cy5-miR-4521@MOF-199 in different organs. Subsequently, the mice were sacrificed, and organs including the heart, liver, spleen, lungs, kidneys, and tumors were collected for ex vivo imaging.

In vivo Assessment of Antitumor Efficacy

The HGC-27 tumor-bearing mice were allocated into four groups. The mice in each group were respectively injected with saline, miR-4521, MOF-199, and miR-4521@MOF-199. The dosage of MOF-199 was 10 mg/kg. The tumor volume was monitored periodically and calculated as (length × width^2)/2. After the experiment ended, the tumors of the mice were collected for measurement and weighing, and then subjected to H&E staining.

Statistical Analysis

Statistical analyses were performed using GraphPad Prism 9 (GraphPad Software, Inc). Comparisons between two groups were conducted using Student's *t*-test, while one-way ANOVA was employed for multi-group comparisons. Results were presented as mean ± SEM, and P-values <0.05 were considered statistically significant.

Results and Discussion

Synthesis and Characterization of miR-4521@MOF-199 NPs

The MOF-199 was fabricated with slight adjustments in accordance with the procedures reported in the literature. SEM images revealed that MOF-199 exhibited a regular octahedral morphology, measuring approximately 100 nm in size, rendering it suitable for biological applications (Figure S1). Subsequently, we loaded miR-4521 mimic into MOF-199 to form miR-4521@MOF-199 NPs (Figure 1A). It is widely acknowledged that the amount of miRNA loaded plays a crucial role in the therapeutic effect. Therefore, we mixed different amounts of miR-4521 with MOF-199 separately and investigated the loading capacity of MOF-199 to load miR-4521 by PAGE. The intensity of the miR-4521 bands was gradually enhanced with the incremental loading of miR-4521 on MOF-199 (Figure 1B), which confirmed that miR-4521 was successfully loaded on MOF-199. The loading capacity of miR-4521 within MOF-199 reached saturation when the weight ratio of miR-4521 to MOF-199 reached 1:44 (w/w), and this loading efficiency was comparable to that reported by Yang et al and Liu et al[34,46] Consequently, a combination of 1 μg miR-4521 with 44 μg MOF-199 was fabricated to form miR-4521@MOF-199 NPs, which were then utilized in the subsequent experiments. Subsequently, we characterized the synthesized miR-4521@MOF-199 NPs. The XRD patterns of both MOF-199 and miR-4521@MOF-199 exhibited identical characteristic peaks to those of the simulated MOF-199, suggesting that the process of miR-4521 loading had no impact on the crystalline structure of MOF-199 (Figure 1C). As shown in Figure 1D and E, TEM images of MOF-199 and miR-4521@MOF-199 revealed a regular morphology and uniform size (~100 nm). DLS analysis

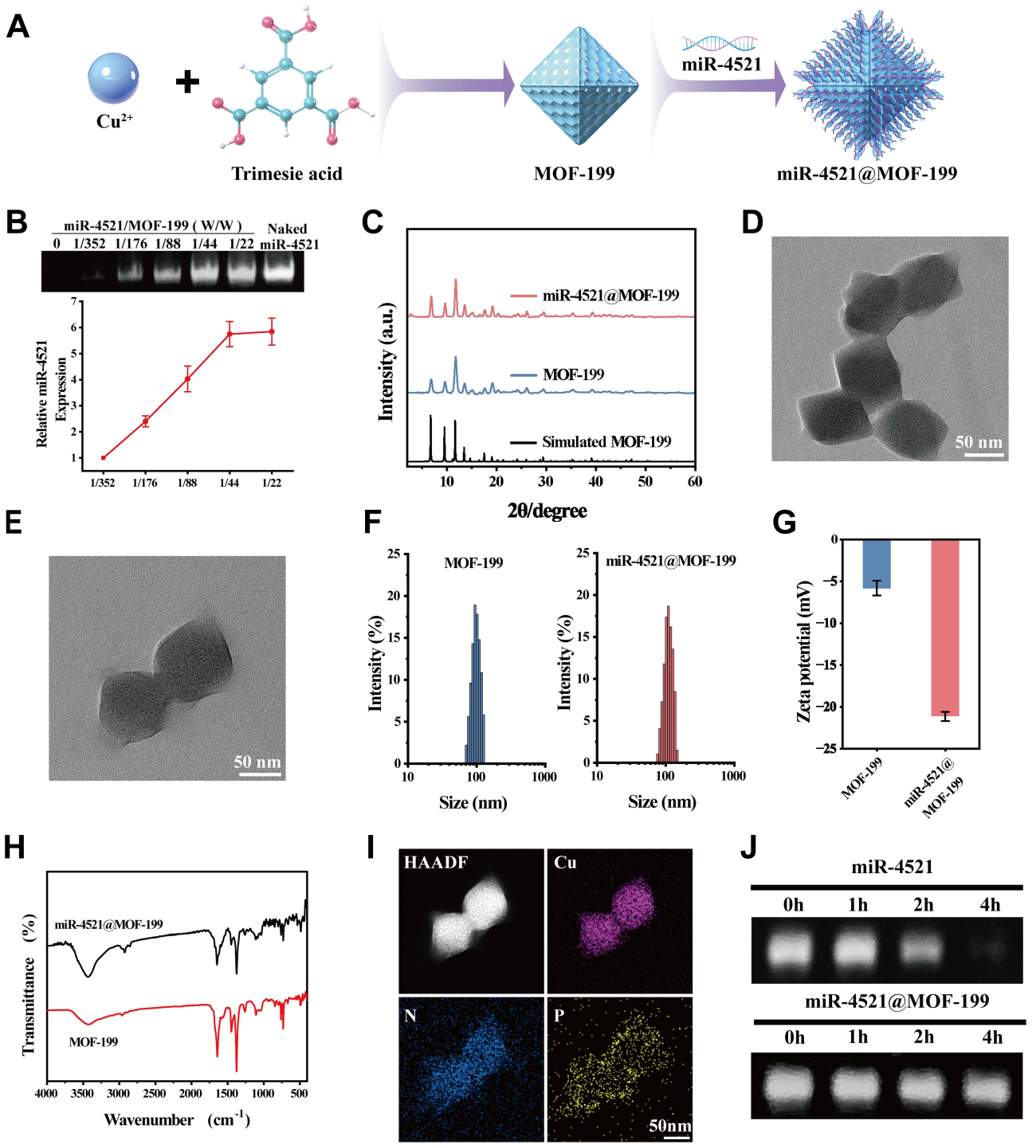

Figure 1 Characterization of miR-4521@MOF-199. (**A**) Preparation process of the miR-4521@MOF-199 NPs. (**B**) The quantity of miR-4521 loaded in miR-4521@MOF-199 with different weight ratios, naked miR-4521 was employed as the reference. (**C**) XRD patterns of MOF-199 and miR-4521@MOF-199. TEM images of (**D**) MOF-199 and (**E**) miR-4521@MOF-199. (**F**) Hydrodynamic diameter of MOF-199 and miR-4521@MOF-199 by DLS. (**G**) Zeta potential of MOF-199 and miR-4521@MOF-199. (**H**) FTIR spectra of MOF-199 and miR-4521@MOF-199. (**I**) HAADF images of miR-4521@MOF-199, and corresponding element mapping: Cu, N, P. (**J**) PAGE results showing the stability of miR-4521 and miR-4521@MOF-199 after incubation in serum for different durations.

revealed that the hydrodynamic diameter of MOF-199 slightly increased from 94.3 ± 3.0 nm to 108.8 ± 5.6 nm after the loading of miRNA (Figure 1F). This is consistent with the TEM results, indicating that the synthesized miR-4521@MOF-199 NPs are of appropriate size and can accumulate at the tumor site via the EPR effect. After miR-4521 was loaded onto MOF-199, the zeta potential changed from −5.8 mV to −21.1 mV, indicating the existence of

https://doi.org/10.2147/IJN.S523766

electrostatic attraction between MOF-199 and miR-4521 (Figure 1G). The FTIR spectrum revealed an additional peak appears at 1619 cm^{-1} for miR-4521@MOF-199, which was caused by the stretching and bending vibrations of the amino N-H groups (Figure 1H). Moreover, the relative intensity of the N-H stretching vibration peak at 3433 cm^{-1} increases significantly, which may be due to the increase in N-H content after miR-4521 loading. Furthermore, the energy dispersive spectroscopy (EDS) mapping image exhibited that Cu (elements in MOF-199), N and P (originating from miR-4521) were homogeneously dispersed within each NP. This observation provided additional evidence for confirming the successful loading of miR-4521 onto MOF-199 (Figure 1I). The stability of miRNAs in circulation is vital for delivery efficiency and therapeutic efficacy. Therefore, the protective effect of miR-4521@MOF-199 on miR-4521 was examined through PAGE. As shown in Figure 1J, the band corresponding to naked miR-4521 nearly disappeared after 4 hours of incubation with serum, indicating that naked miR-4521 is extremely susceptible to degradation by nucleases in the serum. In contrast, the band of miR-4521 in miR-4521@MOF-199 remained clear, indicating that MOF-199 could protect miR-4521 from the degradation of nucleases in serum.

GSH-Triggered Degradation of miR-4521@MOF-199 NPs and Generation of ROS

According to literature reports, copper-based MOF undergo degradation in the microenvironment of tumor cells with a high concentration of GSH, and this degradation process is a prerequisite for drug release.[47,48] Consequently, this study first verified whether GSH could trigger the degradation of miR-4521@MOF-199 NPs. As shown in Figure 2A, with the augmentation of miR-4521@MOF-199 concentration, the characteristic absorbance peak of DTNB at 412 nm declined progressively, which suggests that miR-4521@MOF-199 is capable of consuming GSH. In addition, images of GSH-induced miR-4521@MOF-199 degradation were also observed via TEM. As shown in Figure 2B, the framework of miR-4521@MOF-199 NPs was completely degraded 24 h after the addition of GSH, and the color of the solution changed from blue to white. While the framework of the miR-4521@MOF-199 NPs remained intact 24 h after the addition of PBS. These findings further substantiate the GSH responsiveness of the miR-4521@MOF-199 NP. Subsequently, we

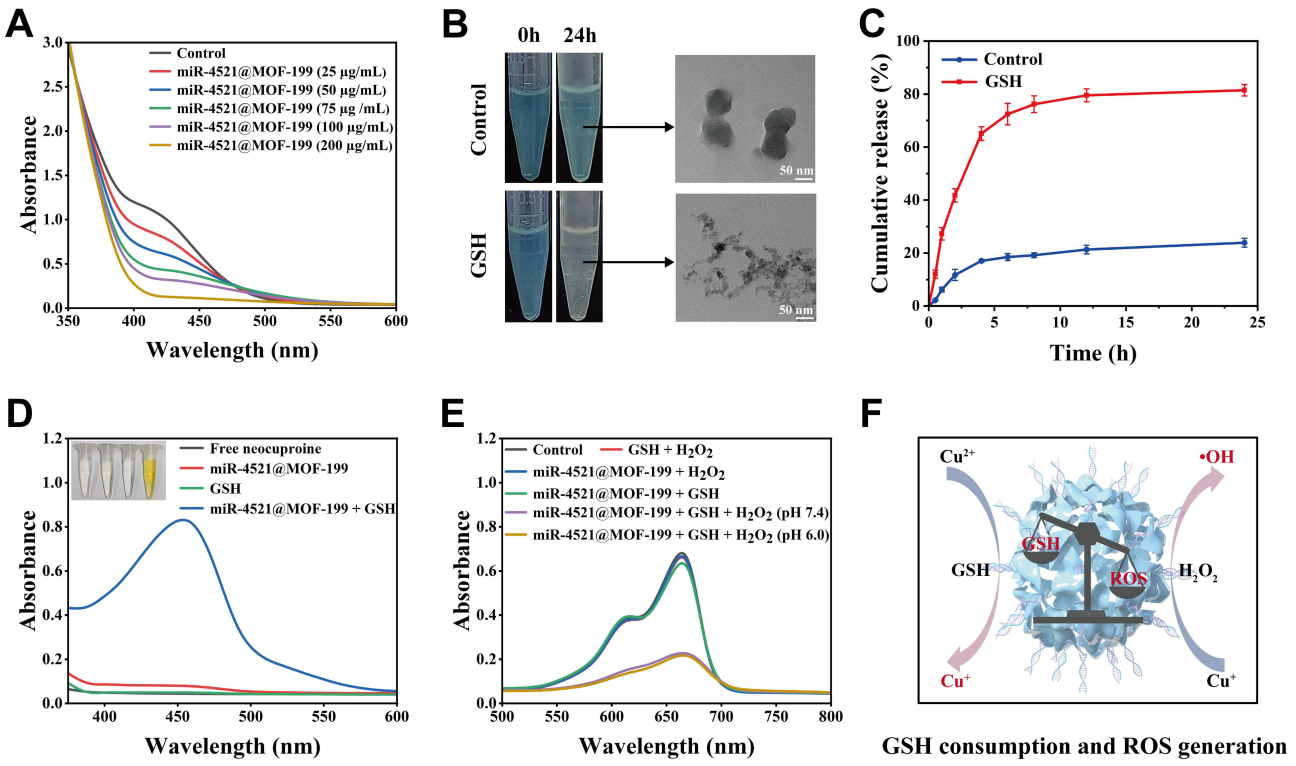

Figure 2 The GSH-responsive and ROS-generating properties of miR-4521@MOF-199. (**A**) UV-vis spectra of GSH under different concentrations of miR-4521@MOF-199. (**B**) Photographs and TEM images of miR-4521@MOF-199 treated with PBS or GSH for 24 h. (**C**) Cumulative release of miR-4521 from miR-4521@MOF-199 in PBS or GSH over time (n = 3). (**D**) UV-vis spectra and photographs of various solutions after neocuproine treatment. (**E**) UV-vis spectra of MB after incubation with different solutions. (**F**) Schematic representation of the mechanism of the Fenton-like reaction induced by miR-4521@MOF-199.

explored the release behavior of miR-4521 from miR-4521@MOF-199 NPs in diverse solutions. The release rate of miR-4521 after 24 h in the GSH solution was approximately 81%, which was much greater than that in the PBS solution (Figure 2C). Furthermore, analyses of miR-4521 release under varying pH conditions demonstrated that pH 6.0 significantly enhanced the release efficiency (Figure S2), indicating that the TME can promote the degradation of miR-4521@MOF-199 NPs. This TME-responsive release property of the miR-4521@MOF-199 NPs has the capacity to attenuate the premature drug release in normal cells and augment drug release in the TME, which is substantially favorable for the abatement of biotoxicity and the amelioration of tumor treatment effectiveness.

Next, we investigated the products after the reaction of miR-4521@MOF-199 with GSH. Upon addition of neocuproine (Cu^+-specific colorimetric indicator) to the mixture of miR-4521@MOF-199 and GSH, the solution exhibited a distinct yellow coloration accompanied by a marked increase in the characteristic absorption peak at 457 nm (Figure 2D). This phenomenon serves as evidence that the reduction product was Cu^+.[48] As a Fenton-like reaction reagent, Cu^+ can transform H_2O_2 in the TME into •OH for CDT.[49] Therefore, methylene blue (MB) was employed as an indicator for the detection of ROS generation. As depicted in Figure 2E, after incubation of miR-4521@MOF-199 with GSH and H_2O_2, the absorbance of MB at 664 nm was noticeably decreased in comparison to that of the other experimental groups. This indicates that in the presence of GSH, miR-4521@MOF-199 could catalyze the production of •OH from H_2O_2 in either neutral or slightly acidic environments. The results demonstrate that under the elevated GSH levels characteristic of tumor cells, miR-4521@MOF-199 undergoes degradation, releasing Cu^{2+} and miR-4521. The Cu^{2+} are reduced to Cu^+ by endogenous reductants (such as GSH), triggering a Fenton-like reaction that converts tumor-overexpressed H_2O_2 into ·OH. This cascade synergistically depletes GSH through redox cycling while generating substantial ROS. This disruptive function to the intracellular redox balance of tumor cells plays a crucial role in the process of killing tumor cells (Figure 2F).

Cellular Uptake and Cytotoxicity of miR-4521@MOF-199 NPs

Effective cellular uptake is a critical determinant of therapeutic efficacy for drug delivery systems. To evaluate the intracellular uptake of miR-4521@MOF-199 NPs, FAM-labeled miR-4521 was employed as a fluorescent tracer. CLSM revealed time-dependent enhancement of green fluorescence intensity in tumor cells (Figure 3A), paralleled by a significant increase in intracellular copper levels following miR-4521@MOF-199 treatment (Figure S3). These results indicate that miR-4521@MOF-199 NPs achieve effective accumulation within tumor cells after 8 h of incubation. We subsequently analyzed the cell internalization efficiency of miR-4521@MOF-199 and naked miR-4521 by CLSM and flow cytometry after 8 h of incubation with tumor cells. Free miR-4521 exhibits a small amount of uptake because it has difficulty crossing the cell membrane (Figures 3B and S4).[50] However, miR-4521@MOF-199 is able to achieve a large amount of uptake through the cellular endocytosis of NPs.[51] These results strongly support that MOF-199 is an ideal nanocarrier for the effective delivery of miR-4521 into cells.

Next, the cytotoxicity of miR-4521@MOF-199 was evaluated via a CCK-8 assay. As shown in Figure 3C and D, the cytotoxicity of naked miR-4521 was low in HGC-27 and AGS cells even at high concentrations (192 nM), possibly because naked miR-4521 is difficult to take up by cells and is easily degraded by nucleases. In contrast, miR-4521@MOF-199 exhibited significant cytotoxicity at lower concentrations (60 μg/mL) and was significantly more cytotoxic than naked miR-4521 and MOF-199 at the same dose, suggesting that miR-4521@MOF-199 synergistically exerts the therapeutic effects of MOF-199 and miR-4521 on tumors. Notably, GES-1 and HUVEC cells retained high viability even after treatment with a high concentration (120 μg/mL) of miR-4521@MOF-199 (Figures 3E and S5), demonstrating its excellent biocompatibility. Subsequently, a live/dead staining assay was used to investigate the antitumor efficacy of miR-4521@MOF-199. As shown in Figure 3F and G, the outcomes demonstrated that the tumor cells which had been treated with miR-4521@MOF-199 presented the greatest quantity of dead cells (red). Flow cytometry analysis revealed that miR-4521@MOF-199 treatment induced apoptosis in 58.87% of HGC-27 cells, a rate significantly higher than other treatment groups (Figure 3H and I). Similar results were observed in AGS cells (Figure S6A and B). Microscopic examination further showed that cell density significantly decreased and morphological alterations occurred after treatment with miR-4521@MOF-199 (Figure S7A). SEM imaging further confirmed the above findings: control cells showed intact membrane structures, while drug-treated cells exhibited characteristics of

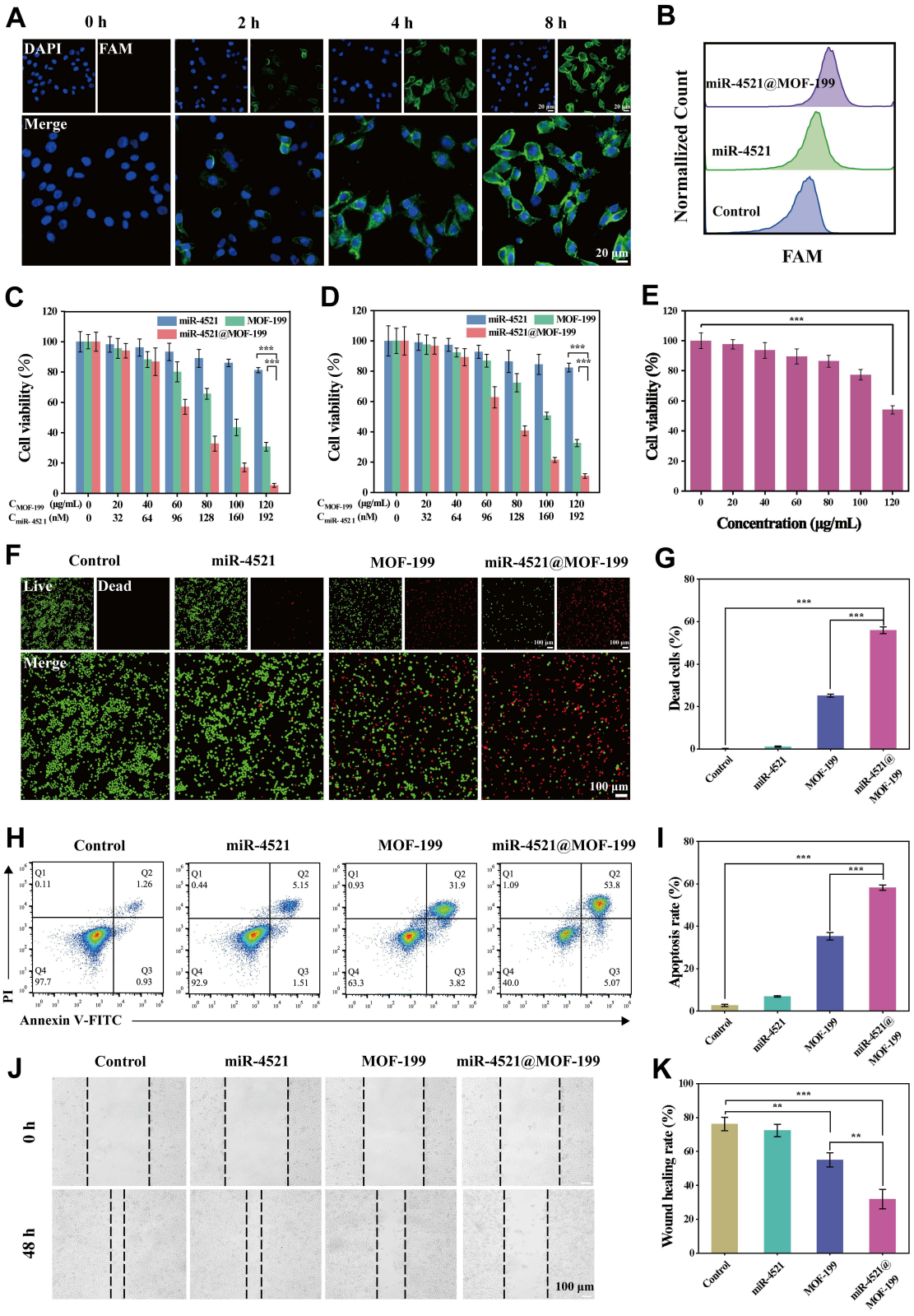

Figure 3 Tumor cell uptake and toxicity analysis of miR-4521@MOF-199. (**A**) Confocal fluorescence images of the uptake of FAM-miR-4521 by HGC-27 cells after incubation with miR-4521@MOF-199 for different times (0 h, 2 h, 4 h, 8 h). (**B**) Flow cytometry analysis of cellular uptake after incubation of miR-4521@MOF-199 with HGC-27 cells for 8 h. (**C** and **D**) Cell viability of HGC-27 and AGS cells after treatment with different drugs. (**E**) Cell viability of GES-1 cells after treatment with different concentrations of miR-4521@MOF-199. (**F** and **G**) Fluorescence images of live/dead assays of HGC-27 cells and statistical analysis (n = 3). (**H** and **I**) Apoptosis detection and statistical analysis of HGC-27 cells treated with PBS, miR-4521, MOF-199, or miR-4521@MOF-199 respectively. (**J** and **K**) Analysis and statistics of the migration ability of HGC-27 cells after different treatments. (**p < 0.01, ***p < 0.001).

pore-like structures (Figure S7B). Additionally, miR-4521@MOF-199 significantly inhibited the migration of HGC-27 cells (Figure 3J and K). These experimental results collectively confirm its potent antitumor function.

Mechanism of miR-4521@MOF-199 NPs Antitumor

Motivated by the outstanding in vitro antitumor performance of miR-4521@MOF-199, we explored its antitumor mechanism. After miR-4521@MOF-199 enters tumor cells, it is degraded by the high concentration of GSH, which is a critical step for miR-4521@MOF-199 to achieve its antitumor efficacy. Therefore, we used a GSH assay kit to detect the intracellular GSH content after treatment with miR-4521@MOF-199. Firstly, a standard curve was constructed following the provided instructions (Figure S8). The variations in the intracellular GSH content after treatment with different concentrations of miR-4521@MOF-199 were subsequently calculated on the basis of this standard curve. As shown in Figure 4A, the amount of intracellular GSH decreased as the concentration of miR-4521@MOF-199 increased, which further demonstrated that miR-4521@MOF-199 was GSH-responsive. Moreover, GSH can reduce Cu^{2+} to Cu^{+} with stronger Fenton activity, so we detected the intracellular ROS content via a ROS indicator (DCFH-DA). HGC-27 and AGS cells treated with naked miR-4521 presented negligible fluorescence intensity, whereas those treated with MOF-199 presented observable green fluorescence, suggesting that MOF-199 can generate ROS in tumor cells (Figures 4B and S9). Notably, the most intense green fluorescence was detected within the cells that had been subjected to treatment with the miR-4521@MOF-199 NPs. Moreover, the results of the quantitative flow cytometry analysis revealed that the ROS level in the miR-4521@MOF-199 group was 1.35 times greater than that in the MOF-199 group (Figures 4C and S10), suggesting that increased levels of miR-4521 in cells can promote the generation of ROS. Previous literature indicates that FOXM1, the target mRNA of miR-4521, is highly expressed in tumor cells.[52,53] FOXM1 plays a crucial role in inhibiting the production of ROS and enhancing the antioxidant capacity of tumor cells, thereby protecting them from oxidative stress.[7,17] Therefore, an elevation in the level of miR-4521 will lead to an increase in ROS levels by inhibiting the expression of FOXM1. We further verified the above experimental conclusions via RT-qPCR and WB experiments. As depicted in Figure 4D and F, miR-4521@MOF-199 treatment significantly suppressed both FOXM1 mRNA and protein expression levels in tumor cells compared to other treatment groups. These results demonstrate that miR-4521@MOF-199 efficiently delivers miR-4521 into tumor cells, silencing FOXM1 expression to compromise oxidative defense mechanisms and mediate antitumor activity. Notably, although FOXM1 downregulation was observed in GES-1 cells post-treatment, no significant cytotoxicity occurred (Figures 3E and S11), likely attributable to the fact that reduced FOXM1 expression does not affect the physiological functions of normal cells.

Excess intracellular Cu^{2+} leads to the downregulation of FDX1 and abnormal aggregation of DLAT, which induces proteotoxic stress and leads to cuproptosis. Our WB experiments revealed that both MOF-199 and miR-4521@MOF-199 significantly downregulated FDX1 protein expression (Figures 4E and S12). Furthermore, distinct DLAT foci were observed in HGC-27 cells upon coincubation with MOF-199 and miR-452@MOF-199, as detected by CLSM, indicating that DLAT underwent oligomerization (Figure 4G). Notably, in terms of the FDX1 protein expression and DLAT oligomerization, no pronounced disparity was detected between the MOF-199 treated group and the miR-4521@MOF-199 treated group. This implies that cuproptosis represents a mode of cell death that is triggered by an overload of intracellular Cu^{2+} and remains uninfluenced by miR-4521. Both ROS-induced severe oxidative stress and cuproptosis can lead to mitochondrial dysfunction. Therefore, JC-1 dye was employed to assess the alterations in the MMP within tumor cells. As the MMP within tumor cells declines, a shift in the fluorescence of JC-1 from red to green takes place. As shown in Figure 4H and I, the lowest red fluorescence (48.5%) and the highest green fluorescence (51.5%) were detected within tumor cells after treatment with miR-4521@MOF-199, which indicates that miR-4521@MOF-199 can induce the strongest mitochondrial disruption in tumor cells. In summary, miR-4521@MOF-199 NPs can synergize with CDT, gene therapy, and cuproptosis to induce the death of tumor cells, demonstrating powerful antitumor efficacy.

Biosafety Evaluation of miR-4521@MOF-199 NPs

Biosafety is a key indicator for further in vivo application of nanomedicines. Therefore, we evaluated the hemocompatibility and biosafety of miR-4521@MOF-199. Different concentrations of miR-4521@MOF-199 were incubated with erythrocytes. UV-vis spectroscopy was subsequently used to measure the supernatant's absorbance at 540 nm. As shown in Figure 5A, red

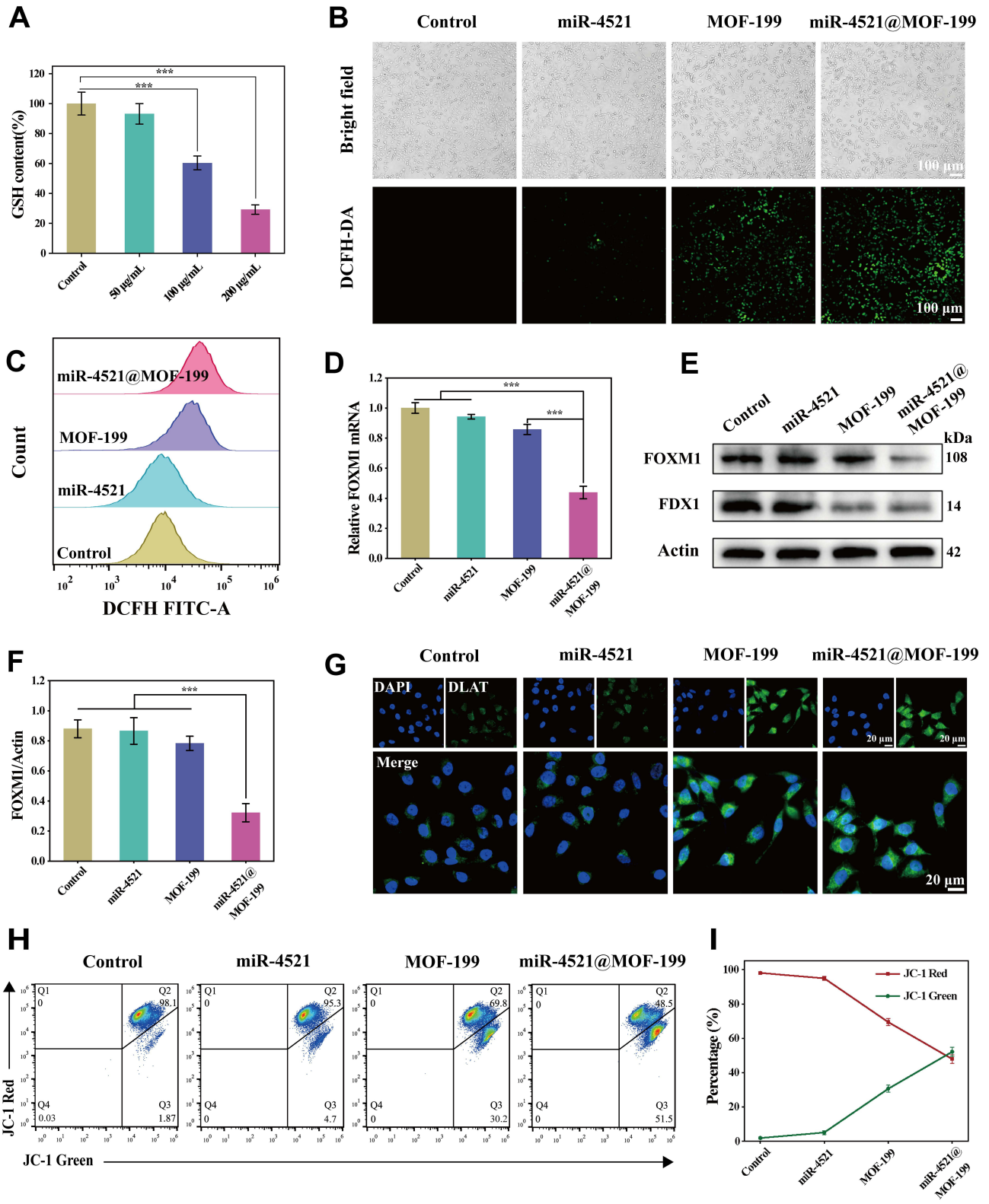

Figure 4 Research on the antitumor mechanism of miR-4521@MOF-199. (**A**) The amount of intracellular GSH in HGC-27 cells subjected to treatments with varying concentrations of miR-4521@MOF-199 (n = 3). (**B**) Fluorescence images of ROS production in HGC-27 cells after various treatments. (**C**) Flow cytometric quantitative analyses of ROS levels in HGC-27 cells after various treatments. (**D**) Analysis of the expression level of FOXM1 mRNA in HGC-27 cells by RT-qPCR after various treatments (n = 3). (**E**) Analysis of the protein expression levels of FOXM1 and FDX1 in HGC-27 cells by WB after different treatments. (**F**) Statistical analysis of the FOXM1 protein (n = 3). (**G**) Immunofluorescence images of DLAT in HGC-27 cells after different treatments. (**H** and **I**) Analysis and statistics of the MMP in HGC-27 cells after different treatments (n = 3). (***p < 0.001).

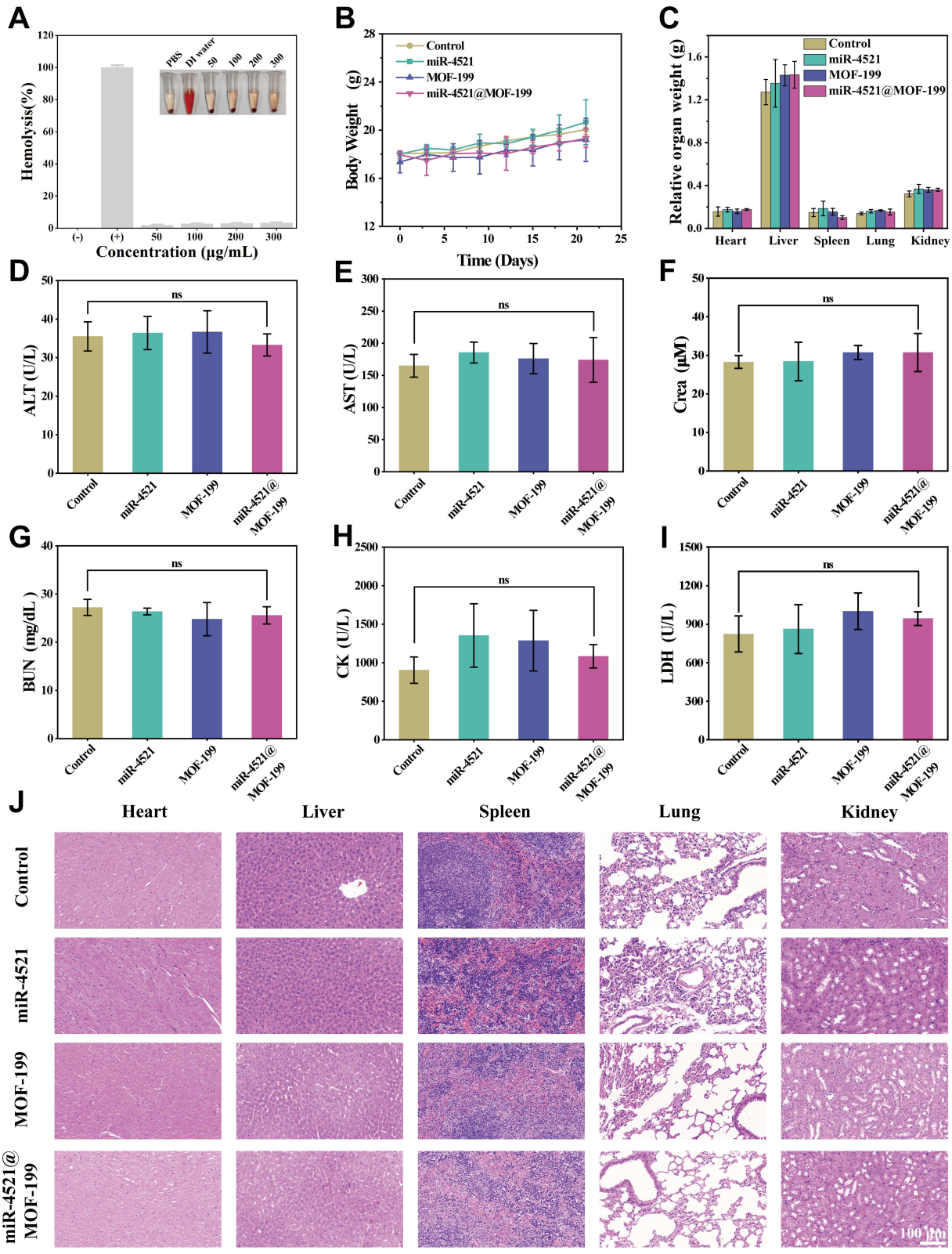

Figure 5 Biosafety of miR-4521@MOF-199. (**A**) Hemolysis analysis of miR-4521@MOF-199 NPs (n = 3). (**B**) Weight changes in healthy Balb/c nude mice after different treatments (n = 3). (**C**) Organ weights of healthy Balb/c nude mice after different treatments (n = 3). (**D–I**) Biochemical assay of serum from healthy mice subjected to various treatments (n = 3). (**J**) H&E staining of vital organs in healthy mice with various treatments. (ns, not significant).

https://doi.org/10.2147/IJN.S523766

blood cells burst and hemolysis occurred after the addition of deionized water. In contrast, the hemolysis rate of erythrocytes treated with miR-4521@MOF-199 remained considerably beneath the clinical safety threshold of 5%, even within the concentration span from 50 to 300 μg/mL. This indicates the favorable hemocompatibility exhibited by miR-4521@MOF-199. Next, PBS, miR-4521, MOF-199, and miR-4521@MOF-199 were administered to healthy mice via the caudal vein. Upon completion of the treatment phase, the blood and organs of the mice were harvested for subsequent examination. The results showed that no pronounced disparity was observed in the body weight and organ weight of the mice subsequent to the treatment with diverse medications (Figure 5B and C). This indicate that miR-4521@MOF-199 has no obvious systemic toxicity. Moreover, the findings regarding the physiological and biochemical parameters of the mouse blood samples indicated that the concentrations of alanine aminotransferase (ALT), aspartate aminotransferase (AST), blood urea nitrogen (BUN), creatinine (Crea), creatine kinase (CK) and lactate dehydrogenase (LDH) in the mice after treatment with miR-4521@MOF-199 were no significantly different from those in the control group (Figure 5D–I). Ultimately, the toxicity of miR-4521@MOF-199 toward the principal organs of healthy mice was further evaluated through H&E staining. The results revealed that no obvious pathological morphological changes such as cell necrosis or inflammation were observed in the mice of each group (Figure 5J). The above results suggest that miR-4521@MOF-199 possesses excellent biocompatibility and is suitable for further in vivo treatment.

In vivo Biodistribution of miR-4521@MOF-199 NPs

After confirming that miR-4521@MOF-199 has excellent antitumor efficacy and biocompatibility, miR-4521@MOF-199 loaded with Cy5-labeled miR-4521 was injected into HGC-27 tumor-bearing mice to further evaluate the biodistribution of miR-4521@MOF-199. As illustrated in Figures 6A and S13A, the fluorescence signal within the tumor region progressively intensified over time. Remarkably, 12 h after injection, a distinct fluorescence signal was detected at the tumor site, whereas the fluorescence at other sites was weak. This indicates that miR-4521@MOF-199 NPs can passively target the tumors via the EPR effect. The fluorescence signal at the tumor site was enhanced at 24 h after injection than at 12 h, indicating that the accumulation of miR-4521@MOF-199 at the tumor site was further enhanced and could be retained at the tumor site. Subsequently, the mice were sacrificed and the tumors along with the principal organs were harvested for the purpose of ex vivo imaging. The results revealed that the fluorescence intensity of the tumor site was greater than that of the other organs (Figures 6B and S13B). Based on these experimental results, we concluded that miR-4521@MOF-199 could be efficiently enriched in tumors through the EPR effect, which is beneficial for in vivo tumor therapy applications.

In vivo Antitumor Efficacy of miR-4521@MOF-199 NPs

Encouraged by the promising in vitro antitumor effects of miR-4521@MOF-199 and its enrichment effect at the tumor site, we further investigated its antitumor efficacy in HGC-27 tumor-bearing mice. Saline, miR-4521, MOF-199, and miR-4521@MOF-199 were injected into HGC-27 tumor-bearing mice via the tail vein every 3 days, and the tumor size was monitored (Figure 6C). As depicted in Figure 6D and E, no marked disparity in tumor volume was noted between the control and miR-4521 groups. This may be because naked miR-4521 has difficulty reaching the tumor site and is easily degraded by nucleases. However, benefiting from the Fenton-like reaction and cuproptosis induced by excessive Cu^{2+}, the tumors in the mice treated with MOF-199 exhibited a degree of shrinkage. Notably, miR-4521@MOF-199 exhibited significant tumor suppression. Photographs of ex vivo tumors showed the same results (Figure 6F). Subsequently, the tumor weight after miR-4521@MOF-199 treatment was only 0.11 g, which was 12.8% of that in the group treated with naked miR-4521 and 25.0% of that in the group treated with MOF-199 (Figure 6G). Furthermore, significant downregulation of FOXM1 mRNA expression was observed in the tumor tissue after treatment with miR-4521@MOF-199 (Figure 6H). These results indicate that miR-4521@MOF-199 can effectively deliver miR-4521 to the tumor site. It then inhibits the expression of FOXM1 mRNA through gene regulation. While exerting a gene therapy effect, it also enhances the toxicity of ROS to tumor cells, thus showing an extremely significant tumor-suppressive effect. Finally, the H&E staining results of the tumors provided clear evidence of profound damage to the tumor tissue subsequent to the treatment with miR-4521@MOF-199 (Figure 6I). This further highlight the remarkable antitumor efficacy of miR-4521@MOF-199. The clinical application of conventional chemotherapeutic agents (such as

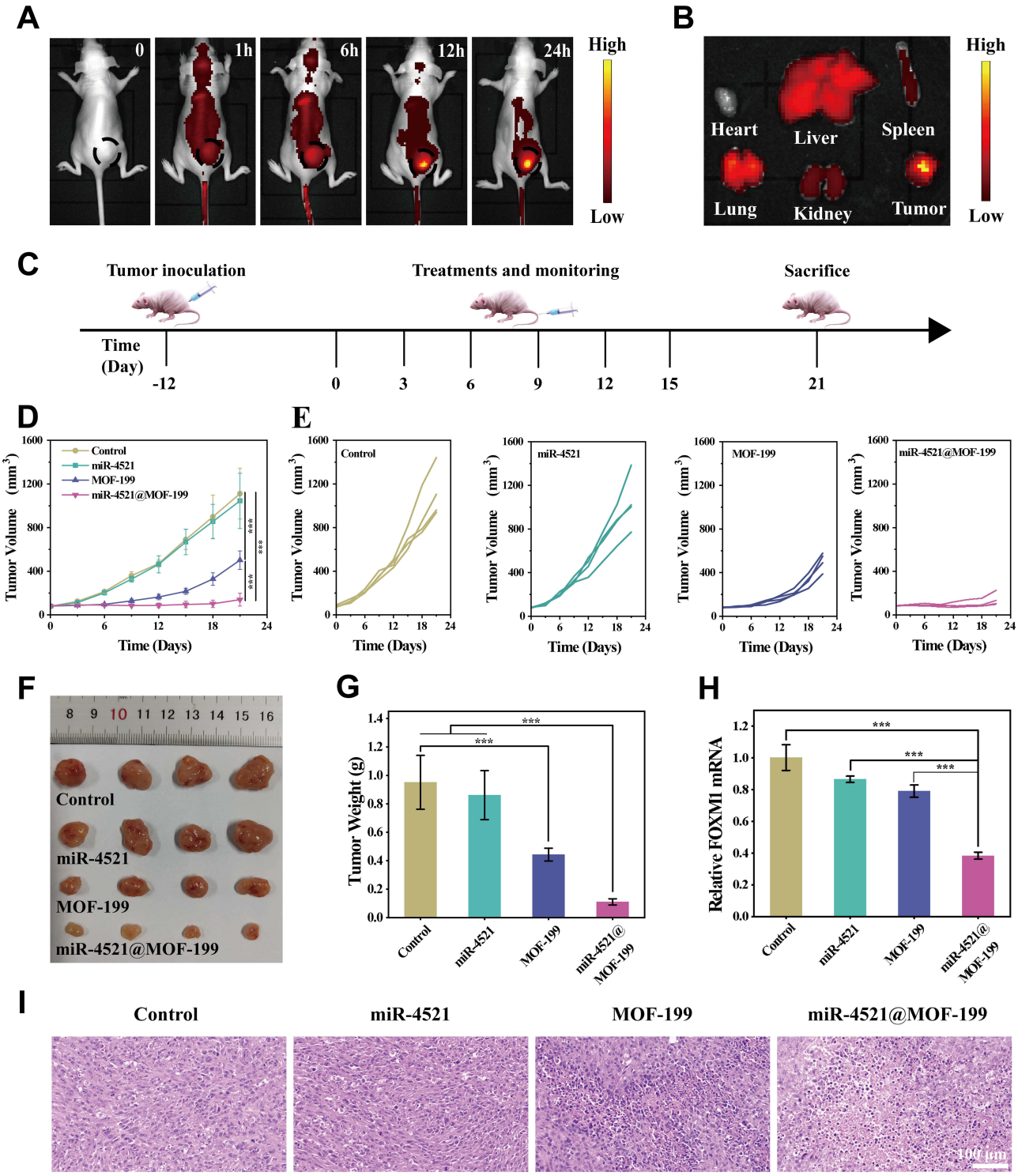

Figure 6 In vivo tumor suppression of miR-4521@MOF-199. (**A**) In vivo fluorescence images of HGC-27 tumor-bearing mice treated with Cy5-miR-4521@MOF-199 at various time points. (**B**) Fluorescent images of tumors and primary organs in mice after 24 h. (**C**) General flowchart of the miR-4521@MOF-199 in vivo experiment. (**D**) Overview of tumor volume in HGC-27 tumor-bearing mice after different treatments (n = 4). (**E**) Tumor volume in each group of HGC-27 tumor-bearing mice after the treatment (n = 4). (**F**) Tumor images and (**G**) tumor weight statistics after different treatments (n = 4). (**H**) RT-qPCR analysis of FOXM1 mRNA in solid tumors after different treatments (n = 4). (**I**) H&E staining analysis of tumor tissues after different treatments. (***p < 0.001).

https://doi.org/10.2147/IJN.S523766

doxorubicin) is significantly constrained by off-target toxicity and drug resistance stemming from monotherapeutic antitumor mechanisms. The miR-4521@MOF-199 NPs enable tumor-specific targeting via the EPR effect, followed by TME-triggered decomposition to release miR-4521. Through synergistic CDT, gene therapy, and cuproptosis, this system demonstrates robust antitumor efficacy and good biosafety.

Conclusion

In summary, we constructed miR-4521@MOF-199 NPs as a TME-responsive miRNA delivery platform for cancer therapy. This multifunctional nanosystem effectively protects and delivers miR-4521 to tumor cells, where elevated GSH levels trigger its degradation, subsequently releasing miR-4521 and Cu^{2+}. The released miR-4521 enhances Cu^{2+}-mediated CDT via gene regulation, while Cu^{2+} induces cuproptosis through proteotoxic stress. In vitro and in vivo experimental results demonstrated that miR-4521@MOF-199 NPs significantly suppress tumor growth while exhibiting high biosafety through the synergistic effects of CDT, gene therapy, and cuproptosis. Considering the complexity and diversity of tumor pathogenesis, this multimodal therapeutic system may provide a promising strategy for cancer treatment.

Acknowledgments

This study was supported by the National Natural Science Foundation of China (Nos. 82060279, 82060161).

Author Contributions

All authors made a significant contribution to the work reported, whether that is in the conception, study design, execution, acquisition of data, analysis and interpretation, or in all these areas; took part in drafting, revising or critically reviewing the article; gave final approval of the version to be published; have agreed on the journal to which the article has been submitted; and agree to be accountable for all aspects of the work.

Disclosure

All the authors of this study declare that there is no conflicts of interest.

References

1. Zhou Y, Fan S, Feng L, Huang X, Chen X. Manipulating intratumoral Fenton chemistry for enhanced chemodynamic and chemodynamic-synergized multimodal therapy. *Adv Mater*. 2021;33(48):e2104223. doi:10.1002/adma.202104223
2. Zhao P, Li H, Bu W. A forward vision for chemodynamic therapy: issues and opportunities. *Angew Chem Int Ed Engl*. 2023;62(7):e202210415. doi:10.1002/anie.202210415
3. Yang F, Fang W, Yang M, et al. Enzyme-loaded glycogen nanoparticles with tumor-targeting activatable host-guest supramolecule for augmented chemodynamic therapy. *Int J Biol Macromol*. 2022;217:878–889. doi:10.1016/j.ijbiomac.2022.07.183
4. Jana D, Zhao Y. Strategies for enhancing cancer chemodynamic therapy performance. *Exploration*. 2022;2(2):20210238. doi:10.1002/exp.20210238
5. Diehn M, Cho RW, Lobo NA, et al. Association of reactive oxygen species levels and radioresistance in cancer stem cells. *Nature*. 2009;458(7239):780–783. doi:10.1038/nature07733
6. Gorrini C, Harris IS, Mak TW. Modulation of oxidative stress as an anticancer strategy. *Nat Rev Drug Discov*. 2013;12(12):931–947. doi:10.1038/nrd4002
7. Choi HJ, Jhe YL, Kim J, et al. FoxM1-dependent and fatty acid oxidation-mediated ROS modulation is a cell-intrinsic drug resistance mechanism in cancer stem-like cells. *Redox Biol*. 2020;36:101589. doi:10.1016/j.redox.2020.101589
8. Calin GA, Croce CM. MicroRNA signatures in human cancers. *Nat Rev Cancer*. 2006;6(11):857–866. doi:10.1038/nrc1997
9. Garzon R, Calin GA, Croce CM. MicroRNAs in Cancer. *Annu Rev Med*. 2009;60:167–179. doi:10.1146/annurev.med.59.053006.104707
10. Croce CM. Causes and consequences of microRNA dysregulation in cancer. *Nat Rev Genet*. 2009;10(10):704–714. doi:10.1038/nrg2634
11. Bartel DP. MicroRNAs: genomics, biogenesis, mechanism, and function. *Cell*. 2004;116(2):281–297. doi:10.1016/s0092-8674(04)00045-5
12. Kasinski AL, Slack FJ. Epigenetics and genetics MicroRNAs en route to the clinic: progress in validating and targeting microRNAs for cancer therapy. *Nat Rev Cancer*. 2011;11(12):849–864. doi:10.1038/nrc3166
13. Rupaimoole R, Slack FJ. MicroRNA therapeutics: towards a new era for the management of cancer and other diseases. *Nat Rev Drug Discov*. 2017;16(3):203–222. doi:10.1038/nrd.2016.246
14. Xing S, Tian Z, Zheng W, et al. Hypoxia downregulated miR-4521 suppresses gastric carcinoma progression through regulation of IGF2 and FOXM1. *Mol Cancer*. 2021;20(1):9. doi:10.1186/s12943-020-01295-2
15. Kuthethur R, Adiga D, Kandettu A, et al. MiR-4521 perturbs FOXM1-mediated DNA damage response in breast cancer. *Front Mol Biosci*. 2023;10:1131433. doi:10.3389/fmolb.2023.1131433

16. Senfter D, Samadaei M, Mader RM, et al. High impact of miRNA-4521 on FOXM1 expression in medulloblastoma. *Cell Death Dis*. 2019;10 (10):696. doi:10.1038/s41419-019-1926-1
17. Park HJ, Carr JR, Wang Z, et al. FoxM1, a critical regulator of oxidative stress during oncogenesis. *EMBO J*. 2009;28(19):2908–2918. doi:10.1038/emboj.2009.239
18. Halasi M, Pandit B, Wang M, Nogueira V, Hay N, Gartel AL. Combination of oxidative stress and FOXM1 inhibitors induces apoptosis in cancer cells and inhibits xenograft tumor growth. *Am J Pathol*. 2013;183(1):257–265. doi:10.1016/j.ajpath.2013.03.012
19. Roca MS, Moccia T, Iannelli F, et al. HDAC class I inhibitor domatinostat sensitizes pancreatic cancer to chemotherapy by targeting cancer stem cell compartment via FOXM1 modulation. *J Exp Clin Cancer Res*. 2022;41(1):83. doi:10.1186/s13046-022-02295-4
20. Pecot CV, Calin GA, Coleman RL, Lopez-Berestein G, Sood AK. RNA interference in the clinic: challenges and future directions. *Nat Rev Cancer*. 2011;11(1):59–67. doi:10.1038/nrc2966
21. Li C, Wang J, Wang Y, et al. Recent progress in drug delivery. *Acta Pharm Sin B*. 2019;9(6):1145–1162. doi:10.1016/j.apsb.2019.08.003
22. Zhang Y, Wang Z, Gemeinhart RA. Progress in microRNA delivery. *J Control Release*. 2013;172(3):962–974. doi:10.1016/j.jconrel.2013.09.015
23. Menon A, Abd-Aziz N, Khalid K, Poh CL, Naidu R. miRNA: a promising therapeutic target in cancer. *Int J Mol Sci*. 2022;23(19):11502. doi:10.3390/ijms231911502
24. Waehler R, Russell SJ, Curiel DT. Engineering targeted viral vectors for gene therapy. *Nat Rev Genet*. 2007;8(8):573–587. doi:10.1038/nrg2141
25. Yin H, Kanasty RL, Eltoukhy AA, Vegas AJ, Dorkin JR, Anderson DG. Non-viral vectors for gene-based therapy. *Nat Rev Genet*. 2014;15 (8):541–555. doi:10.1038/nrg3763
26. Yang H, Qin X, Wang H, et al. An in vivo miRNA delivery system for restoring infarcted myocardium. *ACS Nano*. 2019;13(9):9880–9894. doi:10.1021/acsnano.9b03343
27. Liu X, Sun T, Sun Y, Manshina A, Wang L. Polyoxometalate-based peroxidase-like nanozymes. *Nano Mater Sci*. 2024. doi:10.1016/j.nanoms.2024.03.002
28. Tang T, Wang Z, Guan J. Achievements and challenges of copper-based single-atom catalysts for the reduction of carbon dioxide to C2+ products. *Exploration*. 2023;3(5):20230011. doi:10.1002/exp.20230011
29. Wu MX, Yang YW. Metal-Organic Framework (MOF)-based drug/cargo delivery and cancer therapy. *Adv Mater*. 2017;29(23):1606134. doi:10.1002/adma.201606134
30. Wuttke S, Lismont M, Escudero A, Rungtaweevoranit B, Parak WJ. Positioning metal-organic framework nanoparticles within the context of drug delivery - A comparison with mesoporous silica nanoparticles and dendrimers. *Biomaterials*. 2017;123:172–183. doi:10.1016/j.biomaterials.2017.01.025
31. Zhang H, Zhang J, Li Q, et al. Site-specific MOF-based immunotherapeutic nanoplatforms via synergistic tumor cells-targeted treatment and dendritic cells-targeted immunomodulation. *Biomaterials*. 2020;245:119983. doi:10.1016/j.biomaterials.2020.119983
32. Li Y, Zhang K, Liu P, et al. Encapsulation of plasmid DNA by nanoscale metal-organic frameworks for efficient gene transportation and expression. *Adv Mater*. 2019;31(29):e1901570. doi:10.1002/adma.201901570
33. Zhuang J, Gong H, Zhou J, et al. Targeted gene silencing in vivo by platelet membrane-coated metal-organic framework nanoparticles. *Sci Adv*. 2020;6(13):eaaz6108. doi:10.1126/sciadv.aaz6108
34. Yang H, Han M, Li J, et al. Delivery of miRNAs through metal-organic framework nanoparticles for assisting neural stem cell therapy for ischemic stroke. *ACS Nano*. 2022;16(9):14503–14516. doi:10.1021/acsnano.2c04886
35. Di XJ, Pei ZC, Pei YX, James TD. Tumor microenvironment-oriented MOFs for chemodynamic therapy. *Coord Chem Rev*. 2023;484:215098. doi:10.1016/j.ccr.2023.215098
36. Wang Y, Xu S, Shi L, Teh C, Qi G, Liu B. Cancer-cell-activated in situ synthesis of mitochondria-targeting AIE photosensitizer for precise photodynamic therapy. *Angew Chem Int Ed Engl*. 2021;60(27):14945–14953. doi:10.1002/anie.202017350
37. Liu J, Yuan Y, Cheng Y, et al. Copper-based metal-organic framework overcomes cancer chemoresistance through systemically disrupting dynamically balanced cellular redox homeostasis. *J Am Chem Soc*. 2022;144(11):4799–4809. doi:10.1021/jacs.1c11856
38. Tian H, Zhang M, Jin G, Jiang Y, Luan Y. Cu-MOF chemodynamic nanoplatform via modulating glutathione and H(2)O(2) in tumor microenvironment for amplified cancer therapy. *J Colloid Interface Sci*. 2021;587:358–366. doi:10.1016/j.jcis.2020.12.028
39. Tang M, Ni J, Yue Z, et al. Polyoxometalate-Nanozyme-Integrated Nanomotors (POMotors) for self-propulsion-promoted synergistic photothermal-catalytic tumor therapy. *Angew Chem Int Ed Engl*. 2024;63(6):e202315031. doi:10.1002/anie.202315031
40. Xie J, Yang Y, Gao Y, He J. Cuproptosis: mechanisms and links with cancers. *Mol Cancer*. 2023;22(1):46. doi:10.1186/s12943-023-01732-y
41. Tsvetkov P, Coy S, Petrova B, et al. Copper induces cell death by targeting lipoylated TCA cycle proteins. *Science*. 2022;375(6586):1254–1261. doi:10.1126/science.abf0529
42. Xu Y, Liu SY, Zeng L, et al. An Enzyme-Engineered Nonporous Copper(I) coordination polymer nanoplatform for cuproptosis-based synergistic cancer therapy. *Adv Mater*. 2022;34(43):e2204733. doi:10.1002/adma.202204733
43. Maeda H, Nakamura H, Fang J. The EPR effect for macromolecular drug delivery to solid tumors: improvement of tumor uptake, lowering of systemic toxicity, and distinct tumor imaging in vivo. *Adv Drug Deliv Rev*. 2013;65(1):71–79. doi:10.1016/j.addr.2012.10.002
44. Fang J, Islam W, Maeda H. Exploiting the dynamics of the EPR effect and strategies to improve the therapeutic effects of nanomedicines by using EPR effect enhancers. *Adv Drug Deliv Rev*. 2020;157:142–160. doi:10.1016/j.addr.2020.06.005
45. Huang QX, Liang JL, Chen QW, et al. Metal-organic framework nanoagent induces cuproptosis for effective immunotherapy of malignant glioblastoma. *Nano Today*. 2023;51:101911. doi:10.1016/j.nantod.2023.101911
46. Zhao H, Li T, Yao C, et al. Dual roles of metal-organic frameworks as nanocarriers for miRNA delivery and adjuvants for chemodynamic therapy. *ACS Appl Mater Interfaces*. 2021;13(5):6034–6042. doi:10.1021/acsami.0c21006
47. Zhang K, Meng X, Yang Z, Dong H, Zhang X. Enhanced cancer therapy by hypoxia-responsive copper metal-organic frameworks nanosystem. *Biomaterials*. 2020;258:120278. doi:10.1016/j.biomaterials.2020.120278
48. Wang L, Xu YT, Liu C, et al. Copper-doped MOF-based nanocomposite for GSH depleted chemo/photothermal/chemodynamic combination therapy. *Chem Eng J*. 2022;438:135567. doi:10.1016/j.cej.2022.135567
49. Fu LH, Wan Y, Qi C, et al. Nanocatalytic theranostics with glutathione depletion and enhanced reactive oxygen species generation for efficient cancer therapy. *Adv Mater*. 2021;33(7):e2006892. doi:10.1002/adma.202006892

50. Deprey K, Batistatou N, Kritzer JA. A critical analysis of methods used to investigate the cellular uptake and subcellular localization of RNA therapeutics. *Nucleic Acids Res*. 2020;48(14):7623–7639. doi:10.1093/nar/gkaa576
51. Oh N, Park JH. Endocytosis and exocytosis of nanoparticles in mammalian cells. *Int J Nanomed*. 2014;9(Suppl 1):51–63. doi:10.2147/ijn.S26592
52. Gartel AL. FOXM1 in cancer: interactions and vulnerabilities. *Cancer Res*. 2017;77(12):3135–3139. doi:10.1158/0008-5472.Can-16-3566
53. Khan MA, Khan P, Ahmad A, Fatima M, Nasser MW. FOXM1: a small fox that makes more tracks for cancer progression and metastasis. *Semin Cancer Biol*. 2023;92:1–15. doi:10.1016/j.semcancer.2023.03.007